International Journal of Hydrogen Energy 203 (2026) 153101

Contents lists available at ScienceDirect

International Journal of Hydrogen Energy

journal homepage: www.elsevier.com/locate/he

CFD-based optimization toolchain for channel geometry in PEM fuel cells with novel BPP material

Julian Nicolas Toussaint [a,b,*], Max Paul Mally [c], Simon Mertes [a,b], Stefan Pischinger [a,b]

[a] Chair of Thermodynamics of Mobile Energy Conversion Systems (TME), RWTH Aachen University, Forckenbeckstraße 4, Aachen, 52074, Germany
[b] Center for Mobile Propulsion (CMP), RWTH Aachen University, Forckenbeckstraße 4, Aachen, 52074, Germany
[c] FEV Europe GmbH, Neuenhofstraße 181, Aachen, 52078, Germany

ARTICLE INFO

Keywords:
Fuel cell
Numerical optimization
CFD channel model
PEMFC liquid water distribution
PEMFC channel design
NSGA II algorithm

ABSTRACT

This work presents a generally applicable, physics-based methodology for optimizing flow channel designs in PEM fuel cells using CFD modeling and multi-objective optimization. A fully resolved 3D CFD model was developed to capture the coupled transport and electrochemical phenomena relevant to Proton Exchange Membrane Fuel Cell (PEMFC) operation. The model is grounded in physical laws and requires only two fitting parameters. These parameters were calibrated using a dedicated fitting algorithm developed within this paper, enabling accurate reproduction of the polarization curve, spatial current density distribution along the channel, and liquid water distribution within the cell across the relevant operating range. The validated model was applied to optimize a novel channel geometry for a low-conductivity polymer-based bipolar plate. The optimization revealed a fundamental trade-off between flow uniformity and electrochemical performance. The selected geometry delivers a current density of $j = 1.719\ \frac{A}{cm^2}$, representing an increase of $0.172\ \frac{A}{cm^2}$ compared to the reference design, while optimizing media distribution uniformity and reducing the cell pitch by 0.13 mm compared to the reference design. The successful optimization confirms the insights from individual parameter studies and validates the robustness and general applicability of the approach. The combined workflow of CFD simulation, parameter fitting, and Pareto-based optimization offers a transferable framework for future channel design challenges, especially when novel bipolar plate materials introduce complex physical constraints.

1. Introduction

The main driver of anthropogenic climate change is the increasing concentration of greenhouse gases, in particular carbon dioxide CO_2, which is mainly released when fossil fuels are burned. This causes around two thirds of the anthropogenic greenhouse effect [1]. While many sectors have been able to reduce their emissions since 1990, CO_2 emissions from the transport sector have continued to rise. In 2019, transport accounted for 25% of total EU emissions, of which 71.7% came from road transport [2]. To counteract this, the European Parliament decided in 2023 that only emission-free cars and light commercial vehicles may be registered from 2035, with a reduction in emissions of 50% by 2030 compared to 1990 [3]. For heavy commercial vehicles, an emissions reduction of 30% is planned by 2030 [4]. Heavy commercial vehicles need alternatives to battery electric drives that are superior in terms of charging time and range. Fuel Cells (FCs) offer advantages here thanks to fast refueling and high power densities [5–7], supported by the EU target of installing a hydrogen filling station every 200 km by 2031 [3].

However, a prerequisite for the broad market penetration of FC as an alternative drive concept is a long service life and low-cost FC components and manufacturing processes. The US Department of Energy has defined a service life of 25,000–30,000 h as the target for heavy-duty commercial vehicles (Class 8 tractor-trailers) by 2030. The target for the cost of the FC system is 60–80 $\frac{\$}{kW}$ [8].

In addition to the Membrane Electrode Assembly (MEA), the BPPs of the anode and cathode are an important core group of the Proton Exchange Membrane Fuel Cell (PEMFC). Within a single cell, they are responsible for media management in the cell, i.e. supplying the cathode and anode with reaction gas and removing the produced water from the cell. However, the BPP also plays an important role in the

* Corresponding author at: Chair of Thermodynamics of Mobile Energy Conversion Systems (TME), RWTH Aachen University, Forckenbeckstraße 4, Aachen, 52074, Germany.
E-mail addresses: toussaint@tme.rwth-aachen.de (J.N. Toussaint), mally@fev.com (M.P. Mally), mertes_s@tme.rwth-aachen.de (S. Mertes), pischinger_s@tme.rwth-aachen.de (S. Pischinger).
URL: http://www.tme.rwth-aachen.de (J.N. Toussaint).

https://doi.org/10.1016/j.ijhydene.2025.153101
Received 17 September 2025; Received in revised form 14 November 2025; Accepted 17 December 2025
Available online 29 December 2025

thermal management of the cell by dissipating the heat of reaction via a coolant through cooling channels embedded in the BPP. As the electrochemical reactions in the MEA generate electrons that must be efficiently transported to the external circuit, the BPP must ensure low-resistance conduction through both reliable electrical contact to the GDL and sufficient bulk conductivity [9]. The most important requirements for the material and design of the BPP can also be derived from the tasks of the BPP, which can be summarized according to various sources as follows:

- High electrical conductivity (>100 $\frac{S}{cm}$ [10])
- Mechanical stability (flexural strength > 59 MPa [10])
- High corrosion resistance [11]
- Low contact resistances at interfaces [10]
- Cheap and preferably light material [12]
- Simple and inexpensive processing of the material into BPP [12]
- Hydrophobic surface [12]
- Low thermal expansion [12]

Within a FC system, 50% of the costs are attributable to the FC stack, in turn around 30% of their costs are attributable to BPPs and seals [13]. For a potential reduction in system costs, the BPPs are therefore particularly relevant in FC systems or stacks with a high cell count.

In addition to the potential for cost reduction, the BPPs are also a decisive factor for the service life of the FC stack. The aim here is to use a material that is as corrosion-resistant as possible, but at the same time has high mechanical strength with a thin material thickness [9]. The respective prioritization of the required properties of the BPP defines the base material of the BPP and the possible manufacturing processes. However, it should be noted that the requirements for high corrosion resistance and mechanical strength and the manufacturing options required for this are in conflict with a potential reduction in costs. A potential cornerstone for solving this conflict of objectives has been laid by a new type of BPP material, which was developed as part of the publicly funded *BiFoilStack* project. This combines the positive properties of the two most common, metallic and compound-based, BPP materials. As a result, comparatively thin and electrically conductive BPPs can be produced with very good corrosion resistance. The manufacturing process developed for this purpose promises good scalability and continuous production of the BPPs, which can reduce manufacturing costs [14–16].

Previous studies on fuel cell design have primarily focused on the macroscopic configuration of flow fields at the cell level, aiming to improve overall flow distribution and current homogeneity across the active area [14,15,17–19]. At the microscale, various channel cross-section shapes have been investigated with respect to key performance indicators such as pressure drop, reactant distribution, and water management. Among them, trapezoidal channel geometries have emerged as particularly promising due to their favorable trade-off between hydraulic and electrochemical performance [20–26].

However, the influence of individual geometric parameters — such as channel height, width, and the rib-to-channel ratio — has typically been studied under specific operating conditions, making the results highly application-dependent and not generally transferable. Moreover, existing investigations almost exclusively consider conventional BPP materials, such as metallic or graphite-based plates, which exhibit high electrical conductivity [27–33]. As a result, a systematic understanding of how these geometric factors interact with the transport and electrochemical characteristics of emerging, low-conductivity BPP materials — such as polymer composites — is still lacking. This lack of understanding poses a significant barrier to the efficient design and deployment of fuel cells using advanced polymer composite BPPs. Closing this gap is essential for enabling robust, scalable, and cost-effective fuel cell systems that leverage the benefits of alternative materials without compromising performance.

This study addresses this gap by developing and applying a physics-based optimization methodology, using BPPs made of polymer composite materials as a use case. A Computation Fluid Dynamics (CFD) model of a PEMFC is created and validated using experimental data, and subsequently employed to systematically investigate the effect of geometric channel parameters on performance for the novel material. In contrast to prior studies (see [34–36]), the proposed approach is not limited to a single MEA configuration or set of boundary conditions. The underlying CFD model uses only two physically interpretable fitting parameters and is designed for automated calibration, enabling fast adaptation to different experimental setups. This enables not only material-specific analysis but also a systematic and reproducible evaluation framework for future studies, significantly improving the comparability and scalability of channel design optimization.

Furthermore, this work presents a generalizable optimization toolchain based on an NSGA-II algorithm, which couples the electrochemical and fluidic domains. The resulting methodology enables material-aware and transferable flow field design, extending the applicability of design principles to a broader range of emerging BPP materials.

2. Methodology

2.1. Definition of target criteria for design evaluation

The evaluation of a channel design for bipolar plates requires the consideration of various performance indicators and target values that significantly influence the functionality and efficiency of the overall system. The indicators most frequently considered in literature are presented below.

Power density. The power density is an essential metric for characterizing a FC stack. The cell pitch, i.e. the total height of the individual FC components, plays a decisive role here. In order to achieve a high power density, it is desirable to design the components as thin as possible [9].

Distribution of the reactants. Ultimately, a homogeneous distribution of the media oxygen O_2 at the cathode and hydrogen H_2 at the anode is crucial for a homogeneous distribution of the current density.

Ohmic losses. Ohmic losses are caused by the conductivity of the materials and the contact resistances between the individual components.

Pressure loss. On the one hand, a low pressure loss through the channels of the BPP and thus through the stack is desirable. On the other hand, Zubel et al. [14,15] have shown that a target pressure loss may be required to achieve uniform media distribution throughout the stack, in accordance with system-level constraints.

Liquid water removal capability. While adequate membrane moisture is required to ensure efficient ionic conductivity, excessive water accumulation may result in channel flooding and localized performance losses, especially at higher current densities.

Mechanical stress. The optimal tensioning of the stack is crucial for the safe and long-lasting operation of a PEMFC, as it influences the internal resistance, gas transport and sealing effect [37–40]. The GDL is compressed, which improves its electrical and thermal conductivity, while its ohmic resistance decreases exponentially with increasing pressure [41,42]. However, excessive compression reduces gas permeability and makes mass transport more difficult [43]. The channel design of the BPP plays a crucial role in ensuring uniform tension and helps to prevent mechanical damage to the GDL [44,45]. In addition, the stiffness of the BPP material — especially in the case of compound materials — must be taken into account, as it influences the pressure distribution in the stack and thus the mechanical stability.

Manufacturability and economic factors. Material and production-related boundary conditions have a significant influence on the manufacturability of flow fields and channel designs of the BPP and must be taken into account in the early design phase. In addition, the choice of material has a direct influence on costs and must be optimized from an economic point of view [14–16].

In the works of Zubel et al. [14,15], conducted within the publicly funded project *BiFoilStack*, aspects such as pressure loss, mechanical stress, manufacturability, and economic factors have already been addressed. Therefore, this paper focuses on the detailed design of the channels within the FC with regard to optimizing the target criteria: power density, distribution of reactants, and liquid water removal capability.

2.2. Model development

The 3D CFD simulation model for a channel within the designed cell design is built in the commercially available software Siemens STAR-CCM+2406 (19.04.007-R8) and is executed on the CLAIX-2023 HPC computing cluster of the RWTH Aachen University on two computing nodes, each with two Intel Xeon 8468 Sapphire (48 cores each; 2.1 GHz) with 256 GB RAM. Basic multidimensional transport mechanisms are resolved within the software after appropriate selection. The prevailing physical mechanisms, which are relevant for modeling within a PEMFC, are supplemented by user-defined formulations from the literature. The following assumptions are made for the modeling:

- Due to the symmetry boundary condition, only one half of the channel is simulated.
- A steady-state approach is used, as transient effects are beyond the design scope.
- The flow within the gas channels is modeled as laminar.
- The behavior of gaseous media is described by the ideal gas law.
- Within the gas channels and the porous layers, a multiphase flow is modeled with the Mixture Multiphase (MMP) model.
- For the gaseous phase, a multi-component mixture consisting of N_2, O_2 and H_2O (cathode side) and H_2, N_2, H_2O (anode side) is assumed.
- A constant density is assumed for the liquid phase.
- The catalyst layers are assumed to be infinitely thin at the interface between the membrane and the Microporous Layer (MPL).
- Cooling is modeled via simplified cooling channels, which are traversed by BASF FCG20 coolant at an inlet temperature of 80 °C and an inlet velocity of 4 $\frac{\mathrm{m}}{\mathrm{s}}$ (see Fig. 1(b), dark gray area).

In Fig. 1 the two geometries to be investigated including the meshing of this study are shown, whereby the geometry in Fig. 1(a) is used for the validation of the model and the geometry in Fig. 1(b) for further investigations. The mesh configuration was adopted from Schmitz et al. [34], who performed a comprehensive mesh independence study for a geometrically equivalent setup. The employed grid was originally designed for transient simulations and thus provides sufficient spatial resolution to accurately capture local transport phenomena. This ensures numerical consistency and allows the present steady-state framework to be readily extended to transient operation if required in future studies.

The geometric dimensions are modeled parametrically so that the individual components on the cathode and anode side can be individually adapted. This parameterization is also taken into account during meshing in order to enable scaling of the mesh with the geometric dimensions.

The meshing is carried out with the '*Quadrilateral Mesher*' using the '*Directed Mesh Method*'. A base size of 0.2 mm is defined for the cells in the BPPs, flow channels and GDLs. At the corners of the flow channels-GDL-BPP, the computational grid is refined to 10% of the base size. The MPLs are cross-linked in the form of a geometric series in which the cell thickness of the computational grid decreases from the GDL to the cell thickness of the membrane. The membrane is resolved very finely with a '*base size*' of $1.5 \cdot 10^{-3}$ mm in order to accurately model the complex transport mechanisms.

2.3. Governing equations

Gas channel. The underlying equations within the gas channels are used to predict the distribution of velocity $\boldsymbol{v}$, pressure p, temperature T, the supplied and discharged media. They are formulated according to [47] for a multi-component mixture with the respective mass fraction Y_i of each component and include the continuity equation, the momentum balance and the conservation of energy:

$$\underbrace{\oint_A \rho Y_i \boldsymbol{v} \cdot d\boldsymbol{a}}_{\text{Convective term}} = \underbrace{\oint_A \boldsymbol{J}_i \cdot d\boldsymbol{a}}_{\text{Diffusive term}} \tag{1}$$

$$\oint_A \rho \boldsymbol{v} \otimes \boldsymbol{v} \cdot d\boldsymbol{a} = -\oint_A p\boldsymbol{I} \cdot d\boldsymbol{a} + \oint_A \boldsymbol{T} \cdot d\boldsymbol{a} \tag{2}$$

$$\oint_A \rho H \boldsymbol{v} \cdot d\boldsymbol{a} = -\oint_A \dot{\boldsymbol{q}} \cdot d\boldsymbol{a} + \oint_A \boldsymbol{T} \cdot \boldsymbol{v} \cdot d\boldsymbol{a} \tag{3}$$

where ρ is the density, A denotes the surface area over which the integration is performed, $\boldsymbol{I}$ is the identity tensor, $\boldsymbol{J}_i$ represents the diffusive flux of species i, H is the enthalpy, $\dot{\boldsymbol{q}}$ is the heat flux vector, and $\boldsymbol{T}$ is the stress tensor.

Porous layers. Within the porous layers (GDLs and MPLs), diffusive mass transport is dominant (see Eq. (1)). The continuity equation assumes a modified form with the formulation of the superficial velocity $\boldsymbol{v}_s$ and the effective diffusion coefficient $\boldsymbol{J}_{\text{eff, i}}$ (see [48,49]):

$$\oint_A \rho Y_i \boldsymbol{v}_s \cdot d\boldsymbol{a} = \oint_A \boldsymbol{J}_{\text{eff}} \cdot d\boldsymbol{a} \tag{4}$$

$$\text{with:} \quad \boldsymbol{v}_s = \chi \cdot \boldsymbol{v}, \tag{5}$$

$$\boldsymbol{J}_{\text{eff, i}} = \frac{\chi}{\tau} \boldsymbol{J}_i \tag{6}$$

$$\chi = \frac{V_f}{V}, \tag{7}$$

where χ is the porosity, τ the tortuosity, V_f the pore volume, and V the total volume.

A generally accepted physical formulation of tortuosity does not exist in literature. Shen et al. [50] have investigated various approaches for determining tortuosity. Yu et al. [51] determined the tortuosity values mathematically for a catalyst layer based on experimentally determined diffusion coefficients. Vetter et al. [52] set up an empirical equation to determine the tortuosity for a commercially available gas diffusion layer of the type SGL 24 DA. With the approach according to Bruggeman [53], the tortuosity can be determined as a function of porosity. For this study, a relationship for the tortuosity based on Bruggeman is formulated (see Eq. (8)). According to Bruggeman, the value is $\varsigma = 0.5$ [53]. For this study, the parameter ς is used to fit the polarization curve to the measured data. The previously described literature can be used to physically plausibilize the result of ς.

$$\tau = \chi^{\varsigma} \tag{8}$$

The momentum conservation equation (see Eq. (2)) is extended by the two source terms to account for the additional pressure loss f_p with the resistance tensor P and the capillary forces f_{cap} (see [54]):

$$f_p = -P \cdot \boldsymbol{v}_s \tag{9}$$

$$P = P_v + P_i |\boldsymbol{v}_s| \tag{10}$$

$$\text{with:} \quad P_{\text{v, gas/liquid}} = \frac{\mu}{K \alpha^{\beta}_{\text{gas/liquid}}}, \tag{11}$$

where P_v is the porous resistance tensor, P_i the inertial resistance tensor, μ the dynamic viscosity, K the permeability of liquid water, α the volume fraction of gas or liquid phase, and β the volume exponent.

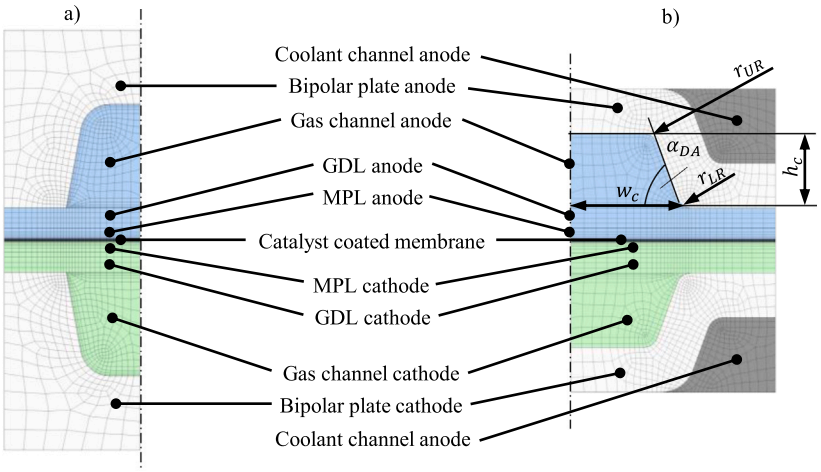

Fig. 1. (a) Geometry of validation geometry [46] (b) Geometry of the investigated geometry [14,15].

The capillary forces f_{cap} are modeled based on the approach of Leverett [55,56].

$$f_{\text{cap, gas/liquid}} = \pm\alpha_{\text{gas}}\alpha_{\text{liquid}}\sigma\cos\left(\frac{\theta_c\pi}{180°}\right)\sqrt{\frac{\chi}{K}}\cdot \nabla\left(1.417\cdot\alpha_{\text{liquid}} - 2.120\cdot\alpha_{\text{liquid}}^2 + 1.263\cdot\alpha_{\text{liquid}}^3\right) \tag{12}$$

where σ is the surface tension between gas and liquid, and θ_c is the contact angle.

Catalyst layers. The electrochemistry is modeled in the assumed infinitely thin interface between the MPL and the cell membrane. Although the catalyst layers are not resolved explicitly in the computational domain, their effects are accounted for through the effective exchange current density and surface area. This approach assumes that intra-layer transport limitations (e.g., protonic resistance, oxygen diffusion through the ionomer phase, and liquid water effects) are lumped into the empirical kinetic parameters. Furthermore, the model has been developed specifically for the purpose of design assessment and optimization, where a good balance between computational cost and physical fidelity is essential. In this context, the primary focus lies on ensuring an adequate three-dimensional supply of reactants and removal of products up to the catalyst layer interface, which is fully resolved in the model. A fully resolved three-dimensional catalyst-layer model would significantly increase the computational expense and is typically required only for detailed studies of electrode materials or Catalyst Layer (CL) microstructure effects. For this purpose, the relationship between the species-specific molar flux $N_{n,s,i}$ — where n denotes the direction normal to the reaction surface s, and i indicates the chemical species — and the local current density $j_{n,s}$ is formulated as source and sink terms of the reactive components using Faraday's law [57] and Strong's law [58]:

$$N_{n,s,i} = \frac{\nu_i}{F\nu_e} j_{n,s} \tag{13}$$

where F is the Faraday constant, ν_i is the stoichiometric coefficient of the reaction component i, and ν_e is the stoichiometric coefficient of the electron.

The correlation between current density $j_{n,s}$ and overpotential at the reactive layer η is described by the Butler–Volmer equation (see Table 1 and [59–63]):

$$j_{n,s} = j_0\prod_i\left(\frac{c_i}{c_{i,\text{ ref}}}\right)^{\gamma_i}\cdot \left(\exp\left(\frac{\alpha_a F\eta}{RT}\right) - \exp\left(\frac{\alpha_c F\eta}{RT}\right)\right) \quad , \tag{14}$$

$$j_0 = j_{0,c/a}^{\text{ref}} a_{CL}\left(\frac{p_i}{p_{\text{ref}}}\right)^{\gamma_{c/a}}\cdot$$

Table 1
Symbols of Eqs. (14)–(16).

Symbol	Description
a_{CL}	Platinum loading in catalyst layer
c_i	Concentration of species i
$c_{i,\text{ref}}$	Reference concentration of species i
$E_{c/a}$	Activation energy (cathode/anode)
j_0	Exchange current density
$j_{0,c/a}^{\text{ref}}$	Reference exchange current density (cathode/anode)
p_i	Partial pressure of component i
p_{ref}	Reference pressure
R	Ideal gas constant
T_{ref}	Reference temperature
α_a	Charge transfer coefficient (anode)
α_c	Charge transfer coefficient (cathode)
$\gamma_{c/a}$	Reaction rate constant (cathode/anode)

$$\exp\left[-\frac{E_{c/a}}{RT}\left(1-\frac{T}{T_{\text{ref}}}\right)\right] \quad , \tag{15}$$

$$\alpha_c = 0.495 + 2.3\cdot 10^{-3}\,(T-300) \quad , \tag{16}$$

Membrane. The membrane is capable of absorbing and desorbing gaseous and liquid water. The sorption equations implemented in STAR-CCM+ are used for this purpose. A distinction is made between the interaction of the gaseous phase with the membrane $r_{\text{surf, Gas}\rightleftharpoons\text{Membrane}}$ (see Eq. (18)) and the interaction between the liquid phase and the membrane $r_{\text{surf, Liquid}\rightleftharpoons\text{Membrane}}$ [48].

$$a_{\text{sorbed}} = \begin{cases} \dfrac{cRT}{p_{\text{sat}}}, & \text{for the gas phase} \\ c, & \text{for the liquid phase} \end{cases} \tag{17}$$

$$r_{\text{surf,Gas}\rightleftharpoons\text{Membrane}} = r_{\text{surf,0}}\left(C_{eq} - a_{\text{sorbed}}\right) \tag{18}$$

$$\text{with:}\quad C_{eq} = \xi\lambda_{eq}, \quad \xi = \frac{\rho_{\text{mem}}}{EW} \quad , [59] \tag{19}$$

$$\lambda_{eq} = 36\cdot a_{H_2O}^3 - 39.85\cdot a_{H_2O}^2 + 17.81\cdot a_{H_2O} + 0.043, \quad \text{for } a_{H_2O}\le 1 \quad , [64] \tag{20}$$

$$r_{\text{surf,Liquid}\rightleftharpoons\text{Membrane}} = r_{\text{surf,0}}\left(He a_{\text{liquid}} - a_{\text{sorbed}}\right) \tag{21}$$

where a is the activity, c the concentration, p_{sat} the saturation vapor pressure, $r_{\text{surf,0}}$ the sorption rate constant, C_{eq} the equilibrium concentration term, ξ the equilibrium concentration constant, ρ_{mem} the membrane density, EW the equivalent weight of the membrane, λ_{eq} the membrane water content at equilibrium, and He the Henry constant.

Various transport processes take place within the membrane. While it is assumed that the membrane is not conductive for electrons, H^+

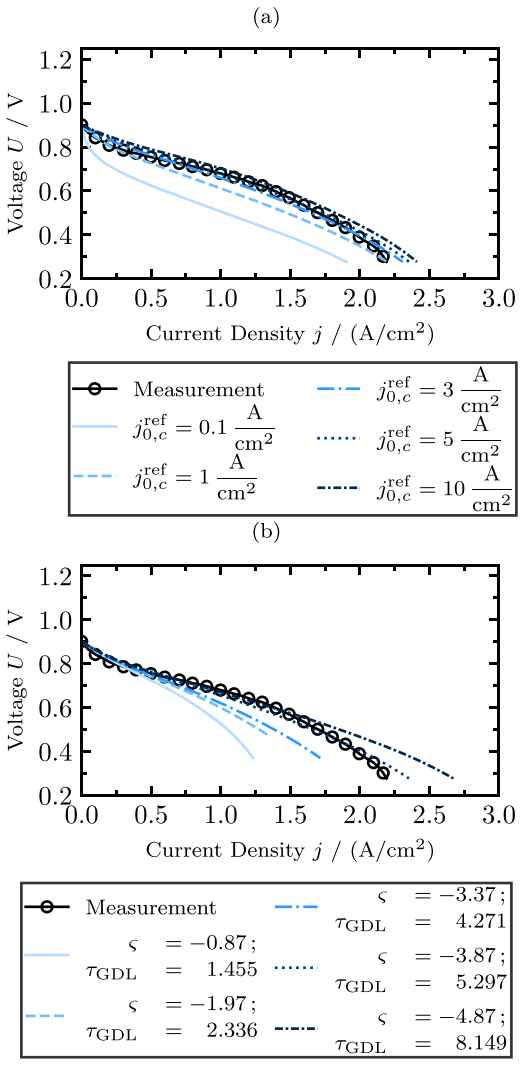

Fig. 2. Comparison of variation of (a) $j_{0,c}^{\mathrm{ref}}$ and (b) τ.

ions are transported through the membrane according to Eq. (22) [64] (see [65]):

$$\sigma_{Mem} = (0.5139 \cdot \lambda - 0.326) \cdot \exp\frac{1}{303} - \frac{1}{T} \tag{22}$$

with: $$\lambda = \frac{EW}{\rho_{\mathrm{Mem}}} c_{\mathrm{H_2O}}\ , \tag{23}$$

where σ_{Mem} is the protonic conductivity of the membrane and λ is the membrane water content (number of water molecules per sulfonic acid group).

The diffusive mass transport of water and the electroosmotic drag are also taken into account [66]:

$$0 = -\nabla\left(-M_{\mathrm{H_2O}} \frac{\rho_{\mathrm{Mem}}}{EW} J_{\mathrm{H_2O\to Mem}} \cdot \nabla\lambda + M_{\mathrm{H_2O}} \frac{n_d}{F} \mathbf{i}_{prot}\right) \tag{24}$$

where M denotes the molecular weight.

The left part of equation Eq. (24) describes the water transport by diffusion with the diffusion coefficient $J_{\mathrm{H_2O\to Mem}}$. This is determined according to [64,67]:

$$J_{\mathrm{H_2O\to Mem}} = \begin{cases} J_0\left(2.563 - 0.33 \cdot \lambda + 0.0264 \cdot \lambda^2 - 0.000671 \cdot \lambda^3\right), & \lambda > 4 \\ J_0\left(-1.25 \cdot \lambda + 6.65\right), & 3 < \lambda \le 4 \\ J_0\left(2.05 \cdot \lambda - 3.25\right), & 2 \le \lambda \le 3 \end{cases} \tag{25}$$

The right part of Eq. (24) describes the electroosmotic drag with n_d [56]:

$$n_d = \frac{2.5}{22}\lambda \tag{26}$$

Electron conductivity. The '*Electromagnetism Model*' implemented in Star-CCM+ describes the conduction of electrons using Maxwell's equations [68–70]. The corresponding conductivities of the individual components such as GDL and BPP can also be taken into account (for material properties, see Appendix B). The contact resistance R_c between BPP and GDL is calculated using the model according to Zhou et al. [71] in dependence of the Compression pressure p_{comp}:

$$R_c = \frac{1}{A_a} A_c \left(\frac{B_c}{p_{\mathrm{comp}}}\right)^{C_c} \tag{27}$$

where A_a is the contact area, A_c, B_c, and C_c are empirical parameters.

All parameters and material properties can be found in Tables 1 and 3 in the appendix.

2.4. Validation strategy

While the reference exchange current density $j_{0,a}^{\mathrm{ref}}$ on the anode side is set to a value of $j_{0,a}^{\mathrm{ref}} = 8\ \frac{\mathrm{A}}{\mathrm{cm}^2}$ due to the much higher reaction rate of the Hydrogen Oxidation Reaction (HOR) reaction. The reference exchange current density on the cathode side $j_{0,c}^{\mathrm{ref}}$ and the exponent ς for determining the tortuosity according to Eq. (8) are selected as fitting parameters, as these variables are difficult to measure and are therefore determined by comparing simulation and measurement. A validation algorithm is developed for this purpose. The influence of the two parameters on the performance of the FC is shown in Fig. 2. It can be seen that the reference exchange current density $j_{0,c}^{\mathrm{ref}}$ shifts the polarization curve of the FC in the vertical direction and has an influence on the activation polarization (see Fig. 2(a)). The variation of the tortuosity has an influence on the diffusion polarization. This can be seen from the fact that the polarization curve bends downwards at higher values of tortuosity even at lower current densities (see Fig. 2(b)).

The schematic process of the validation algorithm is illustrated in Fig. 3. Two operating points of the polarization curve are selected. At Operating Point 1 (OP 1), the reference exchange current density is first varied. At Operating Point 2 (OP 2), the exponent ς of the Bruggeman equation is then adjusted.

An iterative procedure similar to a damped Newton method is used to adjust the respective parameter to the measurement data. The parameter update takes place according to

$$\phi^{(n+1)} = \phi^{(n)} - \frac{j_{\mathrm{sim}}^{(n)} - j_{\mathrm{meas}}}{j_{\mathrm{sim}}^{(n)} - j_{\mathrm{sim}}^{(n-1)}} \cdot \epsilon_\phi \tag{28}$$

with: $\phi = \begin{cases} j_{0,c}^{\mathrm{ref}}, & \text{for OP1} \\ \varsigma, & \text{for OP2} \end{cases}$

where the fraction is a numerical approximation of the derivative and ϵ_ϕ serves as a damping factor to ensure stable convergence.

Since an adjustment of the respective parameter in OP 1 or OP 2 changes the simulation result at the other operating point, the algorithm is run iteratively until the deviation between measurement and simulation at both operating points no longer exceeds a permissible limit of $\epsilon_{\mathrm{sim,meas}}$ after the respective parameter adjustment.

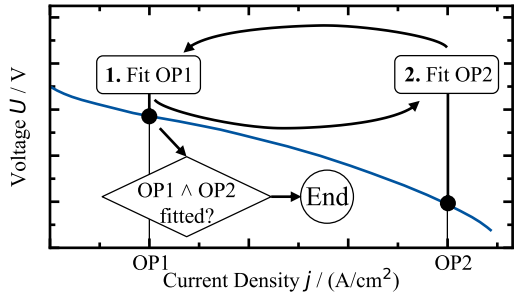

Fig. 3. Validation algorithm.

3. Results

3.1. Validation

The validation process is carried out by transferring the geometric dimensions and material properties of the design used by Fırat [46] into the simulation model. The model is then compared with the measurement data from Schmitz et al. [34] to validate the behavior of the polarization curve.

Since the experimental design is a serpentine design, the channel is modeled as a straight channel with a length of 445.5 mm, as in previous studies by Schmitz [35], extending the previously described model assumptions.

The execution of the validation algorithm leads to a value of the reference exchange current density on the cathode side of $j_{0,c}^{\mathrm{ref}} = 2.4921\ \frac{\mathrm{A}}{\mathrm{m}^2}$ and a value for $\varsigma = -2.17$, resulting in a tortuosity value in the GDL of $\tau_{\mathrm{GDL}} = 2.546$ and in the MPL of $\tau_{\mathrm{MPL}} = 3.261$. Schmitz [35] reported a cathodic exchange current density of the same order of magnitude for the same experimental dataset using a CFD model adapted to cold-start conditions, which further supports the plausibility of the obtained parameter. The values of the derived tortuosity are consistent with the range reported for the SGL 24 DA material, where Vetter et al. [52] derived a tortuosity of $\tau_{\mathrm{GDL}} = 3.191$ based on their empirical model, thereby supporting the plausibility of the results obtained from the present model. These values are consistent with the range reported for the SGL 24 DA material, where Vetter et al. [52] derived a tortuosity of $\tau_{\mathrm{GDL}} = 3.191$ based on their empirical model, thereby supporting the plausibility of the results obtained from the present model.

Fig. 4(a) shows very good agreement between the simulation and measurement results due to the parameters determined. The range of $0.5\ \frac{\mathrm{A}}{\mathrm{cm}^2}$ to $2.0\ \frac{\mathrm{A}}{\mathrm{cm}^2}$ current densities j, which is particularly relevant for the operation of the PEMFC, is captured by the simulation with very high accuracy. Quantitatively, the mean squared error (MSE) between the simulated and measured polarization curve amounts to $1.43 \times 10^{-4}\ \mathrm{V}^2$, corresponding to a root mean squared error (RMSE) of 0.012 V. This deviation corresponds to an average voltage error of about 1–1.5% in the typical operating range of 0.4–0.9 V, indicating an excellent agreement and a high predictive capability of the model. The investigations also show that the model can be operated under both potentiostatic and galvanostatic operating boundary conditions. The latter is particularly relevant for simulative analyses of unknown geometries, as it enables precise adjustment of the stoichiometry during operation.

Polarization curves alone do not provide comprehensive validation for multidimensional PEMFC models. This is because identical integral cell outputs can potentially result from combinations of individually misrepresented submodels [72]. Consequently, high fidelity CFD models require combined global and local validation studies to ensure accuracy. On the one hand, the current density distribution along the channel length is considered locally, which is made possible by the segmented measurement of the test cell (see Fig. 4(b)). The results shown in Fig. 4(b) demonstrate good agreement between simulation and experiment, confirming the model's capability to accurately capture local performance variations along the channel. Quantitatively, the comparison of the measured and simulated current density profiles yields a mean squared error (MSE) of $1.17 \times 10^{-2}\,(\frac{\mathrm{A}}{\mathrm{cm}^2})^2$ and a root mean squared error (RMSE) of $0.108\ \frac{\mathrm{A}}{\mathrm{cm}^2}$. This corresponds to a relative RMSE of approximately 10.1%, indicating that the model reproduces the characteristic current density distribution along the channel with good accuracy, while minor deviations can be attributed to local measurement uncertainties and simplifications in the submodels.

On the other hand, the volumetric liquid water distribution is analyzed using measurement data from previous work by Tabuchi et al. [73] and Corda et al. [74] using Neutron radiography (NRG) visualizations (see Fig. 5). The evaluation line of the CFD simulation runs through the center of the MPL and extends across the entire width of the channel. As the saturation value increases along the channel length direction, several cross-sections at different depths are selected for the analysis. The diagram shows the distribution of the liquid water volume fraction at positions corresponding to 20%, 40%, 60% and 80% of the total channel length l_c.

The liquid water distribution shows a concave profile, indicating a higher degree of saturation in the regions below the ribs compared to the regions below the channel, a pattern that is in high agreement with the results of previous studies, thus confirming the validity of the simulation results.

3.2. Plausibility study

In the next step, the successfully validated model is used to optimize the channel geometry. For this purpose, the channel geometry within the CFD model is adapted to the geometry shown in Fig. 1(b). This geometry was pre-designed in the work of Zubel et al. [14,15] and is to be optimized using the CFD model developed in this paper. An additional challenge arises from the polymer compound used as the BPP material in that work, which exhibits significantly lower electrical conductivity compared to graphitic or metallic materials (approx. 8 times lower than graphite and 100 times lower than stainless steel). This subsequent plausibility study also serves to demonstrate the transferability of the developed modeling and optimization workflow to different material systems, as it is applied to the *BiFoilStack* compound with significantly different electrical and thermal properties compared to the metallic reference.

As a further assumption, the modeling of liquid water was omitted due to the significantly increased computational time it requires. This approach ensures efficient optimization without compromising the accuracy of the final validation, since liquid water effects are most critical in the fully developed operating state and can be reliably evaluated post-optimization. Based on the findings of Liu [75], liquid water tends to accumulate preferentially beneath the ribs, such that wide channels and narrow ribs promote effective water removal.

Fig. 6(a) shows the influence of the BPP material on fuel cell performance. While the black line is retained as a reference for comparison, the colored lines represent the behavior of the fuel cell using the geometry described in Zubel et al. [14,15], but with different BPP materials, in order to quantify the challenges posed by the novel BiFoilStack compound. At the defined design point of $j = 2\ \frac{\mathrm{A}}{\mathrm{cm}^2}$, a voltage difference of approximately 0.1 V is observed between the metallic BPP and the BiFoilStack compound, whereas the graphite-based BPP shows only a slightly lower voltage than the metallic one. The observed voltage difference is primarily driven by the aforementioned higher electrical conductivity of stainless steel, which reduces ohmic losses across the bipolar plate and thus leads to higher cell voltages compared to the composite material.

In Figs. 6(b) and 6(c), the effects on the polarization curve of the BiFoilStack compound material are illustrated for variations in operating pressure on the cathode and anode sides $p_{c/a}$ as well as the stoichiometric ratio of air on the cathode side λ_c, to validate the model behavior. Increasing these operating parameters leads to improved fuel cell performance, which can be attributed to reduced diffusion losses.

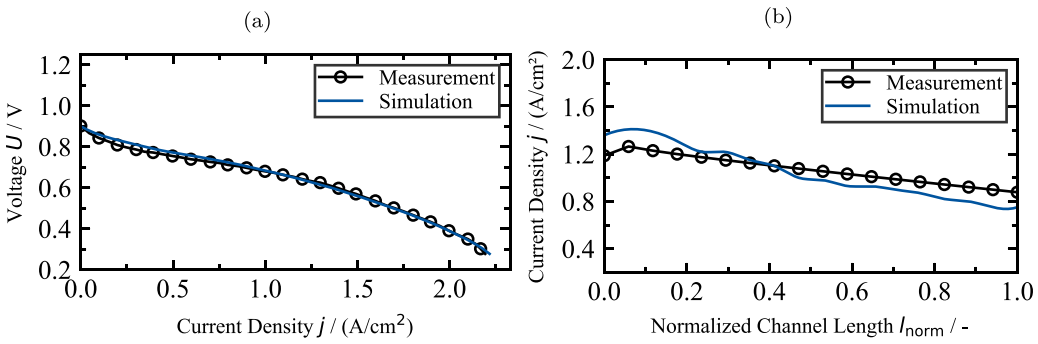

Fig. 4. (a) Results validation polarization curve with $p_{c/a} = 2.0\,\text{bar}$, $\lambda_c = 1.8$, $\lambda_a = 1.6$, $RH = 0.8$, $T = 80°\text{C}$ and (b) Results validation current density in channel length with $U_a = 0.6\,\text{V}$, $p_{c/a} = 1.0\,\text{bar}$, $\lambda_c = 1.8$, $\lambda_a = 1.5$, $RH = 0.6$, $T = 80°\text{C}$.

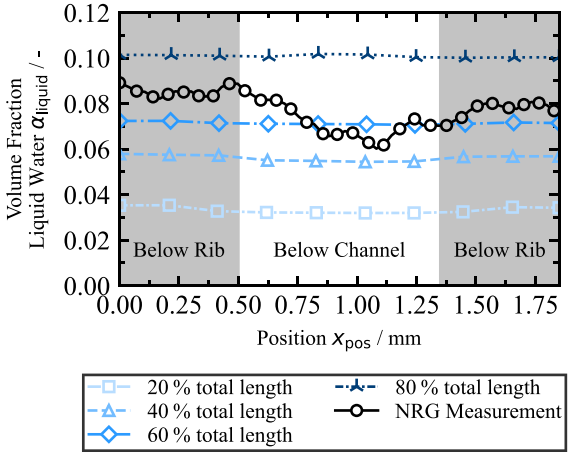

Fig. 5. Validation of liquid water distribution in GDL at $j = 2.5\,\frac{\text{A}}{\text{cm}^2}$.

3.3. Geometry study

To prepare for the optimization of the channel design, the influence of individual geometric parameters on the local current density j (potentiostatic operation of the CFD model), the distribution of the reactants x_{O_2} and x_{H_2}, the pressure drop along the channel, and the uniformity of oxygen O_2 at the catalytically active membrane surface is first investigated for both the cathode and anode channels. The latter is quantified using the uniformity index u_{uni}:

$$u_{\text{uni}} = 1 - \frac{\sigma_{c_{\text{O}_2},\text{mem}}}{\mu_{c_{\text{O}_2},\text{mem}}} \tag{29}$$

where $\sigma_{c_{\text{O}_2},\text{mem}}$ and $\mu_{c_{\text{O}_2},\text{mem}}$ denote the standard deviation and the mean value of the molar oxygen fraction x_{O_2} at the membrane surface, respectively. In this study, all geometric parameters are initially kept constant, and only one parameter is varied at a time to isolate its specific influence. The baseline configuration used for comparison is defined by the default parameter values listed in Table 3 in the appendix and is labeled as the *reference configuration* in the respective diagrams of the investigation. Furthermore, the distribution of the reactants on the catalytic layer is qualitatively analyzed for the lowest and highest values of each geometric variation. This allows for the identification of reactant supply beneath the ribs as well as potential zones of undersupply.

The insights gained from this investigation are intended to support the interpretation of the subsequent channel optimization results. The parameters varied include the draft angle α_{DA}, the channel height h_c, the channel width w_c, as well as the lower and upper channel radii r_{LR} and r_{UR}. The position and definition of the individual geometric parameters are illustrated in Fig. 1(b).

The variation of the draft angle α_{DA} on the cathode side influences the formation of the current density j (see Fig. 7(a)). As the draft angle α_{DA} increases, the supply of reactants to the catalyst layer improves, resulting in a higher molar oxygen fraction x_{O_2} and increased current density (see Fig. 7(b)). This leads to enhanced reactant availability even in the rib regions of the catalyst layer (see Figs. 7(e) and 7(f)). This behavior can be attributed to the higher pressure drop at small draft angles α_{DA} due to the reduced flow cross-section. On the anode side, the influence of the draft angle α_{DA} is negligible. The slightly increased pressure drop at small angles does not significantly affect the reactant supply due to the high diffusivity of hydrogen H_2.

When varying the channel height h_c, a significant influence on the current density j can be observed on both the cathode and anode sides (see Fig. 8(a)). On the cathode side, increasing the channel height from 0.1 mm to 0.4 mm leads to a substantial rise in current density. Further increases beyond 0.4 mm, however, do not result in additional performance improvement. This behavior strongly correlates with the pressure drop Δp_c along the channel, as shown in Fig. 8(c): as the channel height decreases, the pressure drop increases exponentially, significantly impairing the oxygen supply to the catalyst layer (see Figs. 8(b) and 8(d)). As a result, sufficient O_2 supply is observed in the front section of the channel (see Fig. 8(e)), while a growing deficiency occurs toward the channel outlet. At channel heights above 0.4 mm, the pressure drop becomes negligible and no longer limits the reactant supply.

On the anode side, an increase in channel height h_c leads to a slight decrease in the resulting current density j (see Fig. 8(a)). Similar to the cathode side, the pressure drop Δp_c also increases significantly with decreasing channel height (see Fig. 8(c)), albeit at an overall lower level due to the properties of H_2. Despite the increased pressure drop, no relevant undersupply occurs due to the high diffusivity of H_2 (see Figs. 8(b), 8(g), and 8(h)). The observed decrease in current density with increasing channel height is therefore not caused by reactant supply limitations, but results from an increased ohmic resistance within the BPP. The BPP material thus represents the limiting factor in the design of the channel height on the anode side. As already shown in Fig. 6(a), the comparatively low electrical conductivity of the material used imposes specific requirements on the geometric design.

The variation of the channel width $\frac{w_c}{2}$ exhibits a similarly contrasting behavior on both the cathode and anode sides as observed in the variation of the channel height h_c. On the cathode side, increasing the channel width from $0.4\,\text{mm}$ to $1.0\,\text{mm}$ leads to a significant rise in the resulting current density j. As shown in Fig. 9(b), this increase strongly correlates with the improved distribution of the reactant O_2, particularly beneath the ribs. This is primarily due to the shortening diffusion paths for O_2 with increasing channel width (cf. Figs. 9(e) and 9(f)). For narrow channels, e.g., at $0.4\,\text{mm}$, local undersupply of

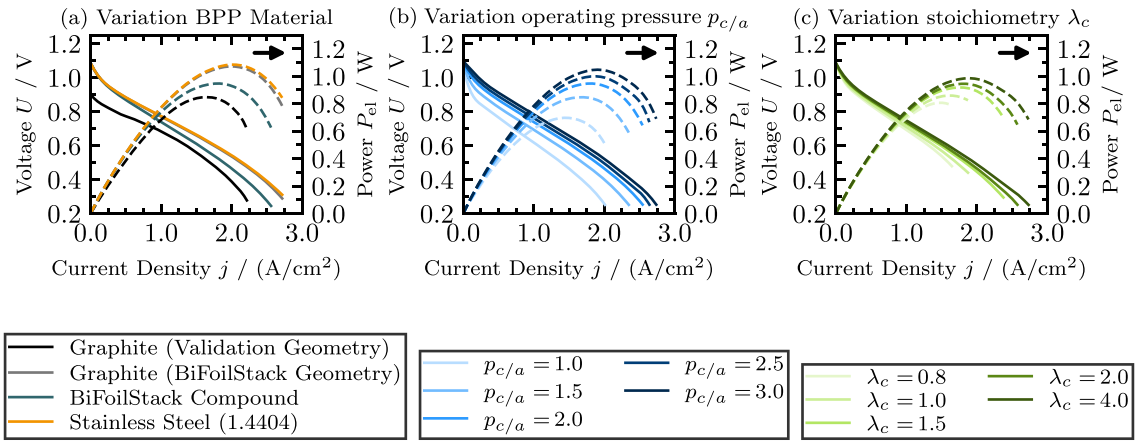

Fig. 6. Variation of BPP Material and operating conditions. (For interpretation of the references to color in this figure legend, the reader is referred to the web version of this article.)

the catalyst layer is observed. In this case, diffusion overpotentials dominate, as oxygen cannot reach the reaction zone quickly enough due to the long diffusion distances.

However, the channel width is limited from above: a further increase beyond 1.0 mm does not lead to an additional increase in current density j. This can be explained by the conflicting objectives of achieving a uniform reactant distribution — favored by wider channels — and minimizing electrical losses—promoted by wider ribs. Beyond a channel width of 1.0 mm, ohmic losses due to the lower conductivity of the BPP as well as contact resistances between the BPP and GDL prevail, limiting further increases in current density.

On the anode side, a behavior similar to that observed in the previously described variation of the channel height can be seen. The primary reason for the increase in current density j with decreasing channel width is the improved electron conduction, resulting from the larger contact area between the BPP and GDL in narrow channels, i.e., wide ribs, which lowers the contact resistance. Despite the high diffusivity of H_2, a slight improvement in reactant supply is observed with increasing channel width (cf. Fig. 9(b)). Nevertheless, none of the investigated variations show critical reactant starvation on the anode side (see Figs. 9(e) and 9(f)).

From Figs. 10 and 11, it can be seen that the variation of the lower radius r_{LR} and the upper radius r_{UR} has no significant impact on the distribution of the current density j. Only in the case of varying the lower radius is a slight decrease in the molar fraction of oxygen x_{O_2} by about one percentage point observed over the investigated range.

For the further investigations on optimizing the channel geometry, variations of the upper and lower radii are omitted. Nevertheless, these geometric parameters should not be neglected in the overall design process. A sufficiently large upper radius of the channel cross-section is crucial to prevent liquid water accumulation. Too small radii promote capillary effects that encourage water droplet adhesion, which can locally obstruct the reactant gas transport. Conversely, a generous rounding facilitates water removal, as droplets can detach more easily from the channel wall and be carried away by the flow. Additionally, the upper radius is subject to manufacturing constraints.

The lower radius is particularly important with regard to the load transfer during the compression of the fuel cell stack, as shown by Liu et al. [45] and Kohrn et al. [76]. Liu et al. [45] propose a parabolic rib contour $h_{\text{surf}}(x)$ according to Eq. (30) to ensure a as uniform as possible stress distribution in the contact area between the BPP and the GDL. The parameter C_1 depends on the rib width d_{rib}, the thickness of the GDL h_{GDL}, and the compression force of the fuel cell stack. Therefore, the design of both radii is finalized within the channel optimization considering mechanical and manufacturing boundary conditions.

$$h_{\text{surf}}(x) = C_1 x^2 + h_{\text{surf}}(0) \tag{30}$$

3.4. Channel optimization

In the course of channel optimization, the final channel structure is designed using the established NSGA-II algorithm. NSGA-II is a widely used evolutionary algorithm specifically developed for multi-objective optimization problems [77]. The NSGA-II algorithm is based on a population-based evolutionary principle, where a set of candidate solutions is optimized simultaneously. It employs a non-dominated sorting approach and a crowding distance method to ensure both convergence and diversity within the solution population. The optimization was executed on the CLAIX-2023 HPC cluster of RWTH Aachen University using two computing nodes, each equipped with two Intel Xeon 8468 Sapphire CPUs (48 cores, 2.1 GHz) and 256 GB RAM. A single simulation required approximately 7 min, resulting in a total computational effort of about 70 core-hours for the complete optimization. Convergence was assessed by monitoring the stabilization of the Pareto front and the crowding-distance distribution over successive generations, which did not change significantly beyond generation 45, indicating convergence of the population. This makes NSGA-II particularly well-suited for problems with multiple competing objectives, as is the case in channel optimization.

For the optimization of the channel structure, the two quantities current density j and uniformity index u_{uni} are used and simultaneously maximized using the NSGA-II algorithm. Since a correlation between pressure drop and current density was observed, the pressure drop is indirectly considered within the optimization objectives. A population size of $N_{\text{Ind}} = 1212$ individuals per generation and a total of $N_{\text{Gen}} = 5050$ generations are chosen for the optimization process, resulting in a total of 600 different design variants.

The channel width is limited to a threshold value of $w_{\text{c,lim}} = 0.68775$ mm based on the investigations by Kohrn [78] in order to avoid excessive intrusion of the GDL into the channels, which can occur with overly wide channels. Such intrusion would lead to increased cell aging and premature mechanical degradation. Although the previous investigations have shown an improvement in current density above $w_{\text{c,lim}}$, this limitation is necessary because otherwise the optimizer could identify a local optimum within this solution space.

The results of the optimization are shown in Fig. 12. The left subfigure (Fig. 12(a)) displays the entire solution space explored by the optimizer, with each circle representing a tested design. The blue shading indicates the performance of each design with respect to the defined objectives — the darker the shade, the better the overall evaluation. The most promising designs are located in the upper right region of the plot. Designs lying on the Pareto front are highlighted in orange and are further detailed in Fig. 12(b). A detailed examination of the Pareto front shows that moving towards higher flow uniformity yields only

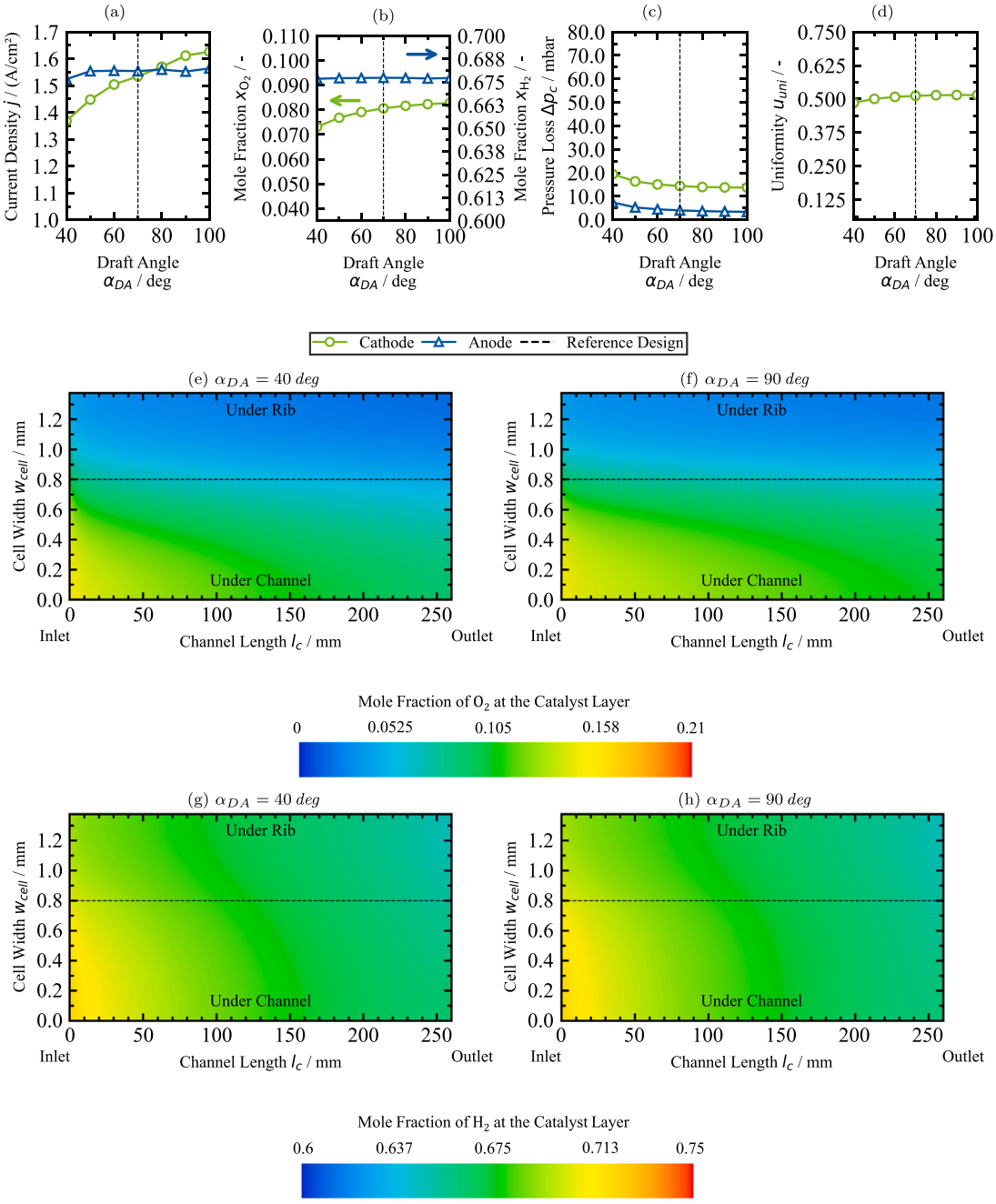

Fig. 7. Geometry study: Effect on draft angle α_{DA}.

marginal improvements in u_{uni} while leading to a noticeable reduction in current density j. Therefore, the optimization reveals a diminishing return when prioritizing uniformity over electrochemical performance. Moreover, an analysis of the Pareto-optimal designs also considered the overall cell height, which was minimized to avoid unnecessary stack growth. This combined assessment led to the selection of design 457 as the optimal compromise.

The distribution of the designs illustrates a classic trade-off: improving flow uniformity consistently results in a reduction of current density. A closer examination of the Pareto-optimal designs reveals that all designs located to the right of design 457 feature increased channel heights on both the anode and cathode sides. This leads to a larger cell pitch and thus an increased total stack height. Against this background, design 457 is selected as the final compromise. It offers a balanced trade-off between the objectives, with a flow uniformity of $u_{\text{uni}} = 0.437$ and a current density of $j = 1.719\ \frac{\text{A}}{\text{cm}^2}$.

Furthermore, it is observed that the gain in current density when selecting a design optimized for this objective is significantly greater than the corresponding gain in uniformity when prioritizing that criterion. Therefore, a design with higher current density is preferred, even at the expense of slightly reduced flow uniformity.

The selection of the final design, 457, confirms not only the findings of the preceding investigations but also validates the overall optimization approach. This underlines the general applicability of the chosen optimization algorithm in the design process of fuel cell channels. The specific values of the geometric parameters are shown in Fig. 12(c). The channel heights are within a range that avoids excessive pressure drops along the flow path. On the cathode side, the channel width approaches the maximum allowable value $w_{\text{c,lim}}$. Compared to the reference design

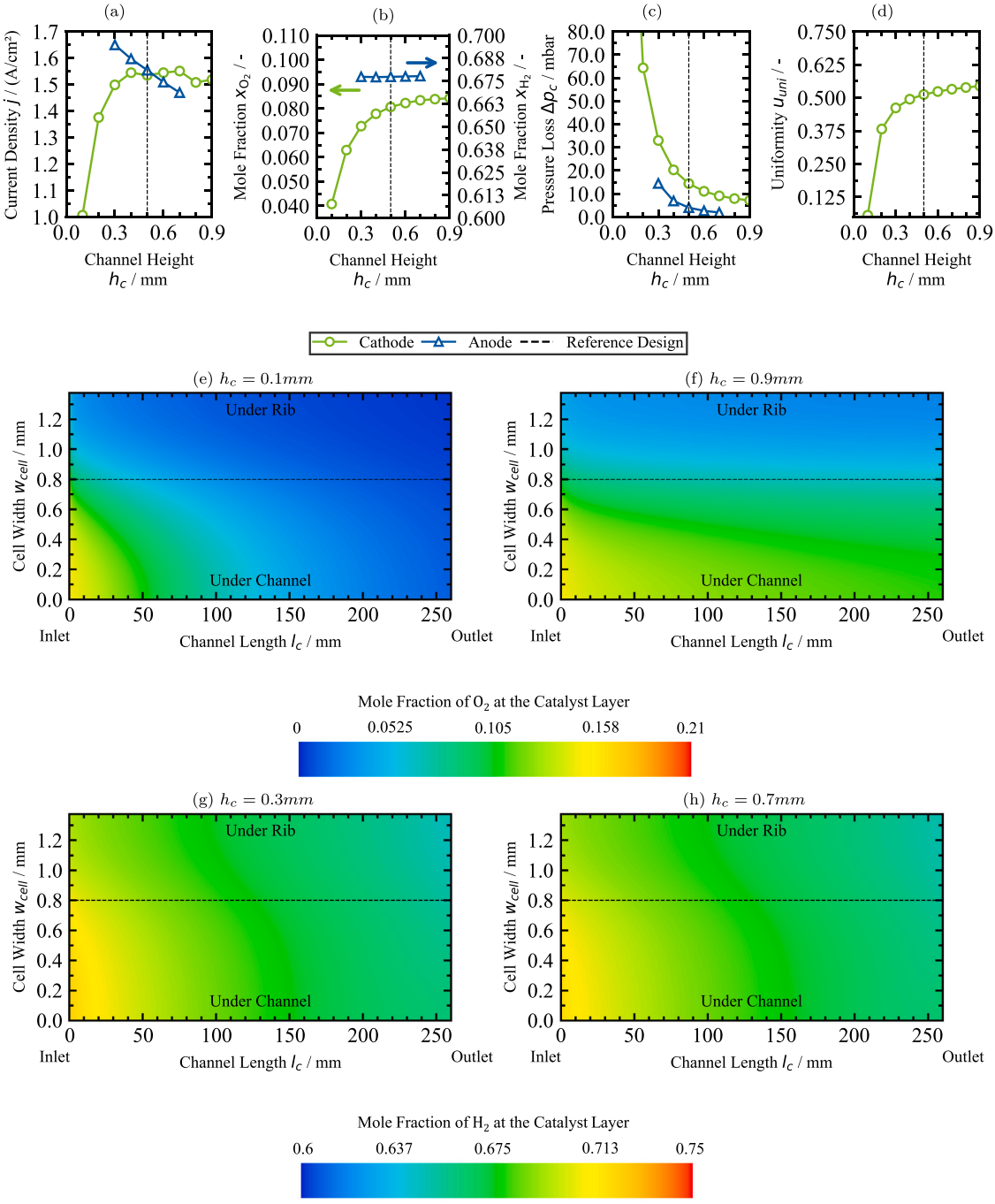

Fig. 8. Geometry study: Effect on channel height h_c.

from the preliminary layout phase, design 457 achieves an increase in current density of $\Delta j = 0.172 \frac{\text{A}}{\text{cm}^2}$, while simultaneously reducing the cell pitch by 0.13 mm.

4. Final design

Fig. 13 shows a comparison of the polarization curves for design variant 457 at an operating pressure of $p = 2.0\,\text{bar}$, which was used for the geometric investigation and optimization, and at the design pressure of $p = 2.88\,\text{bar}$. For reference, the polarization curve of the *BiFoilStack* design is also included in the diagram. Compared to the preliminary design, a uniform increase in the electrical power output P_{el} can be observed across the entire operating range of the FC. At an operating pressure of $p = 2.88\,\text{bar}$, as expected, a further increase in power output is visible over the full operating range. In addition, the blue curve shows the polarization behavior considering liquid water formation. In comparison to the simulation without liquid water, a very small and expected decrease in power output is observed, which can be attributed to local blockages of the three-phase boundary caused by the accumulation of liquid water.

5. Conclusion

This work presents a generally applicable and physics-based methodology for optimizing channel designs in Proton Exchange Membrane Fuel Cell using CFD modeling and multi-objective optimization. A fully resolved 3D CFD model was developed to capture the coupled transport and electrochemical phenomena relevant in Proton Exchange

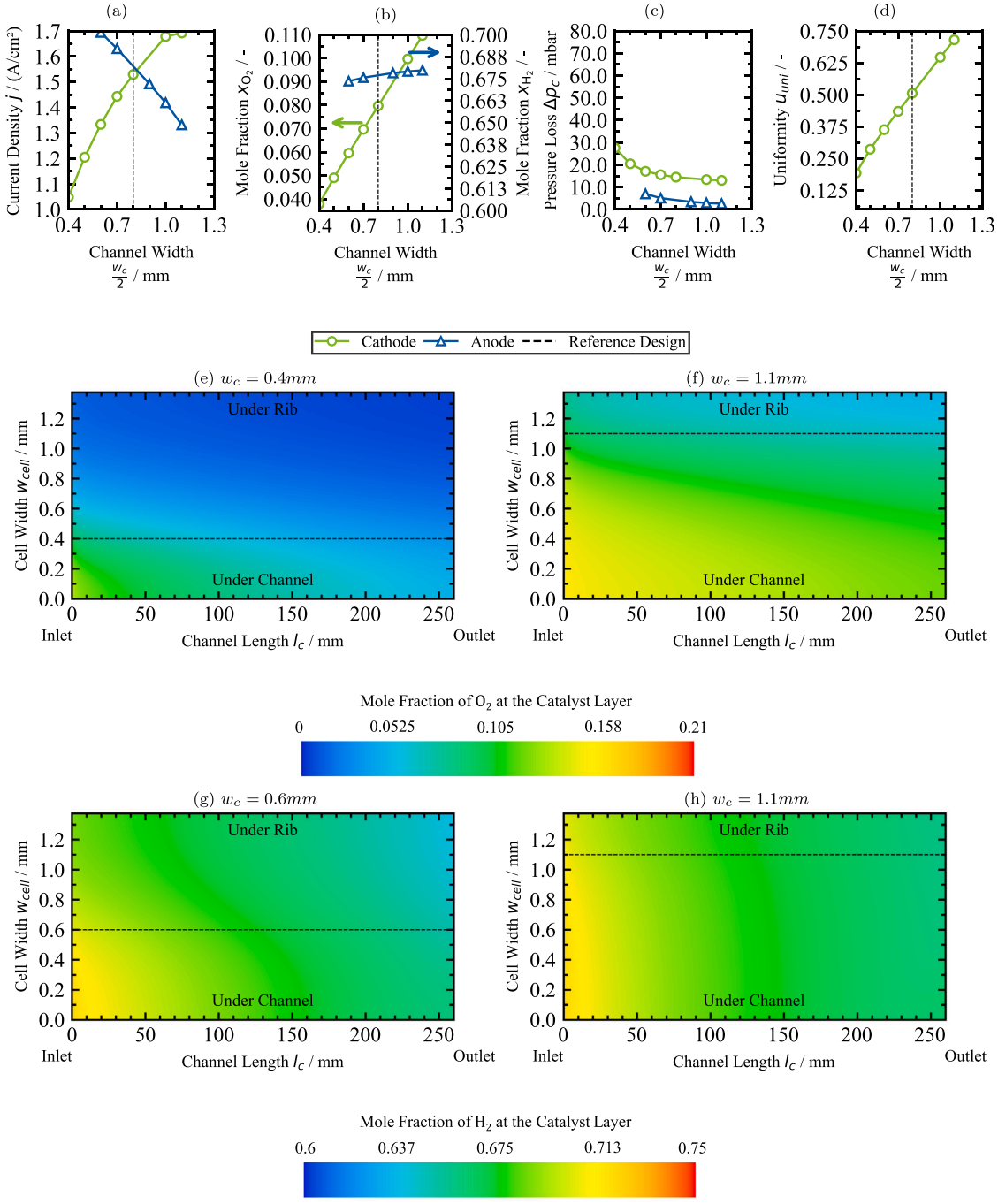

Fig. 9. Geometry study: Effect on channel width w_c.

Membrane Fuel Cell operation. The model is inherently grounded in physical laws and requires only two fitting parameters – the cathodic exchange current density and the Bruggeman exponent to calculate the tortuosity – to adapt it to a specific Membrane Electrode Assembly configuration. These parameters were calibrated using a dedicated fitting algorithm, enabling not only highly accurate reproduction of the polarization curve across the entire application-relevant operating range, but also a precise match of the spatial current density distribution along the channel length and the corresponding liquid water distribution within the cell.

The validated model was then applied to optimize a novel channel geometry designed for a low-conductivity polymer-based bipolar plate. The optimization revealed a fundamental trade-off between flow uniformity and electrochemical performance. The selected geometry achieves a well-balanced compromise, delivering a current density of $j = 1.719\,\frac{\mathrm{A}}{\mathrm{cm}^2}$, which corresponds to an increase of $0.172\,\frac{\mathrm{A}}{\mathrm{cm}^2}$ compared to the reference design, while simultaneously optimizing media distribution uniformity to $u_{\mathrm{uni}} = 0.437$ and reducing the cell pitch by 0.13 mm.

The successful selection of the optimized design not only confirms the insights gained from the investigations of each geometry parameter but also validates the robustness and general applicability of the entire methodological approach. The demonstrated workflow – combining CFD simulation, parameter fitting, and Pareto-based optimization – offers a transferable and scalable framework for future channel design challenges, especially when novel bipolar plate materials impose complex physical constraints. Beyond the scientific findings, the presented workflow provides clear engineering implications. By

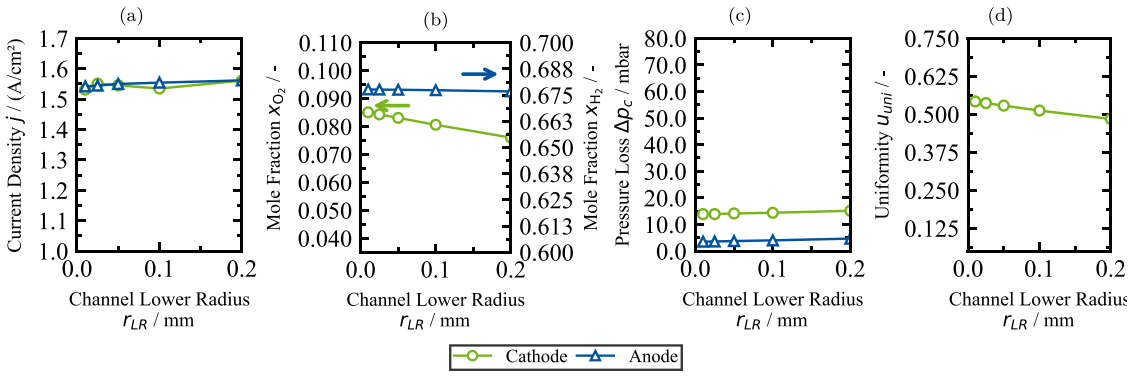

Fig. 10. Geometry study: Effect on lower radius r_{LR}.

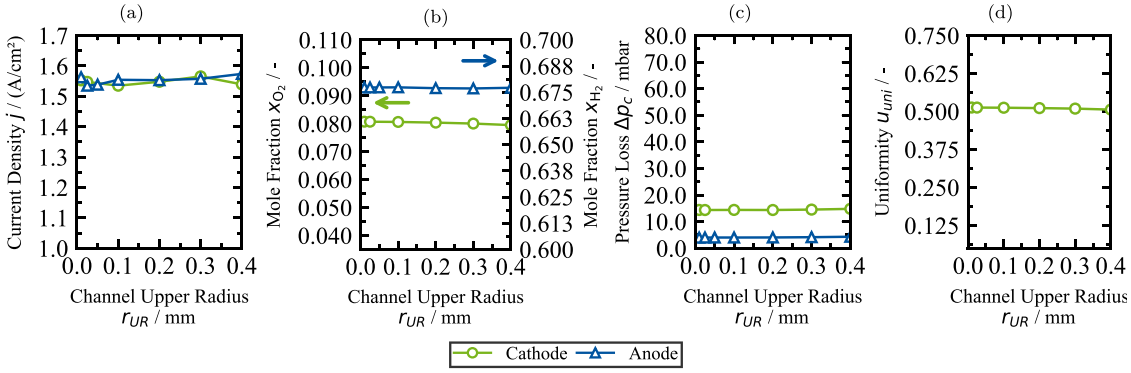

Fig. 11. Geometry study: Effect on upper radius r_{UR}.

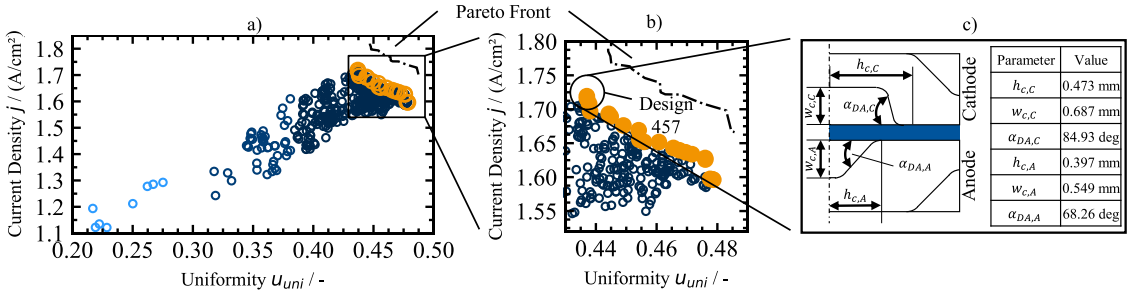

Fig. 12. Results of the optimization. (For interpretation of the references to color in this figure legend, the reader is referred to the web version of this article.)

combining high-fidelity modeling with efficient multi-objective optimization, the approach enables targeted channel design under realistic manufacturability constraints, such as minimum channel widths or rib stability limits. This ensures that the resulting geometries are not only optimal in performance but also feasible for mass production using conventional polymer or metallic bipolar plate manufacturing routes. Furthermore, the reduction in the number of required design iterations directly lowers development time and cost. The method thus offers a viable pathway toward accelerating the industrial adoption of novel low-conductivity or composite bipolar plate materials while maintaining robust fuel cell performance. An experimental validation of the optimized design is planned within the *BiFoilStack* project with a short-stack.

CRediT authorship contribution statement

Julian Nicolas Toussaint: Writing – original draft, Visualization, Validation, Methodology, Investigation, Formal analysis, Data curation, Conceptualization. **Max Paul Mally:** Writing – review & editing, Supervision, Resources, Methodology. **Simon Mertes:** Writing – review & editing, Supervision, Methodology. **Stefan Pischinger:** Writing – review & editing, Supervision, Funding acquisition.

Declaration of competing interest

The authors declare that they have no known competing financial interests or personal relationships that could have appeared to influence the work reported in this paper.

Acknowledgments

This work was conducted within the publicly funded *BiFoilStack* project, supported by the German Federal Ministry for Economic Affairs and Energy (BMWi) under grant number 03EN5018A–D. The authors gratefully acknowledge the computing time provided to them at the NHR Center NHR4CES at RWTH Aachen University (project number p0024400). This is funded by the Federal Ministry of Education and Research, Germany, and the state governments participating on the basis of the resolutions of the GWK for national high performance computing at universities (www.nhr-verein.de/unsere-partner).

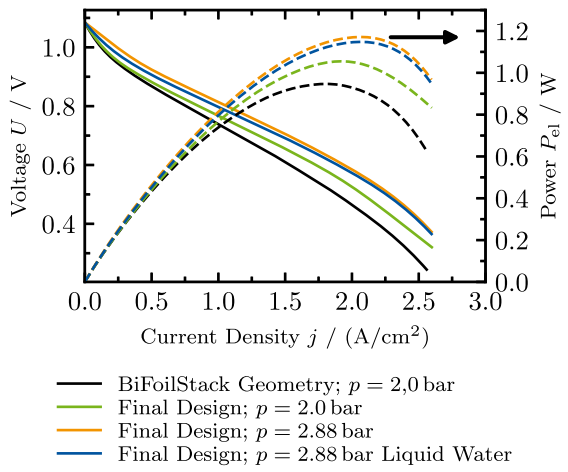

Fig. 13. Investigation of the electrochemical performance of the final design at different cathode-side operating pressures and with consideration of liquid water with $\lambda_a = 1.6$; $\lambda_c = 1.8$; $RH = 0.8$; $T = 80°C$. (For interpretation of the references to color in this figure legend, the reader is referred to the web version of this article.)

Appendix A. Supplementary data

Supplementary material related to this article can be found online at https://doi.org/10.1016/j.ijhydene.2025.153101.

References

[1] Lee H, Romero J. Climate change 2023: Synthesis report: Contribution of working groups I, II and III to the sixth assessment report of the intergovernmental panel on climate change. 2023, http://dx.doi.org/10.59327/IPCC/AR6-9789291691647.

[2] Europäisches Parlament. CO2 emissions from cars: facts and figures (infographic), URL https://www.europarl.europa.eu/news/de/headlines/society/20190313STO31218/co2-emissionen-von-pkw-zahlen-und-fakten-infografik.

[3] Europäisches Parlament. Fit for 55: deal on charging and fuelling stations for alternative fuels, URL https://www.europarl.europa.eu/news/en/press-room/20230327IPR78504/fit-for-55-deal-on-charging-and-fuelling-stations-for-alternative-fuels.

[4] Europäisches Parlament. Parliament confirms new CO2 emission limits for trucks. URL https://www.europarl.europa.eu/news/de/press-room/20190412IPR39009/parlament-bestatigt-neue-co2-emissionsgrenzwerte-fur-lkws.

[5] Cullen DA, Neyerlin KC, Ahluwalia RK, Mukundan R, More KL, Borup RL, Weber AZ, Myers DJ, Kusoglu A. New roads and challenges for fuel cells in heavy-duty transportation. Nat Energy 2021;6(5):462–74. http://dx.doi.org/10.1038/s41560-021-00775-z.

[6] Emran A, Mertes S, Garg S, Wick M, Walters M, Sharma V. Fuel cell electric vehicles - An optimal solution for future electrification of heavy commercial vehicles in India. In: 2021 IEEE transportation electrification conference (ITEC-India). IEEE; 2021, p. 1–8. http://dx.doi.org/10.1109/ITEC-India53713.2021.9932475.

[7] Toussaint JN, Mertes S, Schmidt M, Sterlepper S, Walters M, Pischinger S. Development of a cloud-based toolchain for data science in fuel cell vehicles. J Power Sources 2025;648:237276. http://dx.doi.org/10.1016/j.jpowsour.2025.237276.

[8] Marcinkoski J, Vijayagopal R, Adams J, James B, Kopasz J, Ahluwalia R. Hydrogen class 8 long haul truck targets. 2019.

[9] O'Hayre RP, Cha S-W, Colella WG, Prinz FB. Fuel cell fundamentals. 3rd ed.. Hoboken, New Jersey: Wiley; 2016.

[10] Planes E, Flandin L, Alberola N. Polymer composites bipolar plates for PEMFCs. Energy Procedia 2012;20:311–23. http://dx.doi.org/10.1016/j.egypro.2012.03.031.

[11] Tang A, Crisci L, Bonville L, Jankovic J. An overview of bipolar plates in proton exchange membrane fuel cells. J Renew Sustain Energy 2021;13(2). http://dx.doi.org/10.1063/5.0031447.

[12] Hermann A, Chaudhuri T, Spagnol P. Bipolar plates for PEM fuel cells: A review. Int J Hydrog Energy 2005;30(12):1297–302. http://dx.doi.org/10.1016/j.ijhydene.2005.04.016.

[13] Wang J, Wang H, Fan Y. Techno-Economic challenges of fuel cell commercialization. Engineering 2018;4(3):352–60. http://dx.doi.org/10.1016/j.eng.2018.05.007.

[14] Zubel M, Walters M, Jafari S, Soddemann M, Kadlcak J, Dechent S-E, Laubacher F, Keller P, Ott J, Toussaint J, Joemann M, Huwald L, Wand M. BiFoilStack—Novel cell and stack design with Compound-Foil-Based bipolar plates for Heavy-Duty fuel cell systems. In: Heintzel A, editor. Antriebe und energiesysteme von morgen 2023. Proceedings, Wiesbaden: Springer Fachmedien Wiesbaden; 2025, p. 28–49. http://dx.doi.org/10.1007/978-3-658-46551-3_4.

[15] Zubel M, Walters M, Jafari S, Soddemann M, Kadlcak J, Dechent S-E, Laubacher F, Keller P, Ott J, Toussaint JN, Joemann M, Huwald L, Wand M. BiFoilStack - Novel cell and stack design with Compound-Foil-Based bipolar plates for heavy-duty fuel cell systems. In: Chair of Thermodynamics of Mobile Energy Conversion Systems RWTH Aachen University, Institute for Automotive Engineering RWTH Aachen University, editor. 31st aachen colloquium sustainable mobility 2022. 2022, URL https://publica.fraunhofer.de/handle/publica/428444.

[16] Joemann M, Schwerdt P, Kopietz L, Hackfort T, Bogenstahl F. KONTIFLEX - Kontinuierliche Herstellung neuartiger, flexibler und preisgünstiger Graphit-Bipolarplatten für PEM-Brennstoffzellen : gemeinsamer wissenschaftlich-technischer Schlussbericht : Laufzeit des vorhabens: 01.01.2016 bis 31.12.2018. 2019, http://dx.doi.org/10.2314/KXP:1694303500.

[17] Kahraman H, Orhan MF. Flow field bipolar plates in a proton exchange membrane fuel cell: Analysis & modeling. Energy Convers Manage 2017;133:363–84.

[18] Sauermoser M, Kizilova N, Pollet BG, Kjelstrup S. Flow field patterns for proton exchange membrane fuel cells. Front Energy Res 2020;8. http://dx.doi.org/10.3389/fenrg.2020.00013.

[19] Pedapati PR, Dhanushkodi SR, Chidambaram RK, Taler D, Sobota T, Taler J. Design and manufacturing challenges in PEMFC flow fields—A review. Energies 2024;17(14):3499. http://dx.doi.org/10.3390/en17143499.

[20] Zeng X, Ge Y, Shen J, Zeng L, Liu Z, Liu W. The optimization of channels for a proton exchange membrane fuel cell applying genetic algorithm. Int J Heat Mass Transfer 2017;105:81–9. http://dx.doi.org/10.1016/j.ijheatmasstransfer.2016.09.068.

[21] Paulino ALR, Cunha EF, Robalinho E, Linardi M, Korkischko I, Santiago EI. CFD analysis of PEMFC flow channel cross sections. Fuel Cells 2017;17(1):27–36. http://dx.doi.org/10.1002/fuce.201600141.

[22] Busqué R, Bossio M, Brigido A, Lara A. Effects of different channel geometries of metallic bipolar plates on proton exchange membrane fuel cell performance. Energies 2023;16(23):7702. http://dx.doi.org/10.3390/en16237702.

[23] Chen Z, Yang X, Hu X, Wang C. Optimization of channel structure for proton exchange membrane fuel cells based on a three–dimensional two–phase flow model. Int J Energy Res 2021;45(6):8794–809. http://dx.doi.org/10.1002/er.6415.

[24] Freire LS, Antolini E, Linardi M, Santiago EI, Passos RR. Influence of operational parameters on the performance of PEMFCs with serpentine flow field channels having different (rectangular and trapezoidal) cross-section shape. Int J Hydrog Energy 2014;39(23):12052–60. http://dx.doi.org/10.1016/j.ijhydene.2014.06.041.

[25] Kim J, Kim W. Numerical investigation of Gas-Liquid Two-Phase flow inside PEMFC gas channels with rectangular and trapezoidal cross sections. Energies 2018;11(6):1403. http://dx.doi.org/10.3390/en11061403.

[26] Mohammedi A, Sahli Y, Ben Moussa H. 3D investigation of the channel cross-section configuration effect on the power delivered by PEMFCs with straight channels. Fuel 2020;263:116713. http://dx.doi.org/10.1016/j.fuel.2019.116713.

[27] Carcadea E, Ismail MS, Ingham DB, Patularu L, Schitea D, Marinoiu A, Ion-Ebrasu D, Mocanu D, Varlam M. Effects of geometrical dimensions of flow channels of a large-active-area PEM fuel cell: A CFD study. Int J Hydrog Energy 2021;46(25):13572–82. http://dx.doi.org/10.1016/j.ijhydene.2020.08.150.

[28] Cooper NJ, Smith T, Santamaria AD, Park JW. Experimental optimization of parallel and interdigitated PEMFC flow-field channel geometry. Int J Hydrog Energy 2016;41(2):1213–23. http://dx.doi.org/10.1016/j.ijhydene.2015.11.153.

[29] Ghanbarian A, Kermani MJ. Enhancement of PEM fuel cell performance by flow channel indentation. Energy Convers Manage 2016;110:356–66. http://dx.doi.org/10.1016/j.enconman.2015.12.036.

[30] Goebel SG. Impact of land width and channel span on fuel cell performance. J Power Sources 2011;196(18):7550–4. http://dx.doi.org/10.1016/j.jpowsour.2011.04.005.

[31] Manoj Kumar P, Kolar AK. Effect of cathode channel dimensions on the performance of an air-breathing PEM fuel cell. Int J Therm Sci 2010;49(5):844–57. http://dx.doi.org/10.1016/j.ijthermalsci.2009.12.002.

[32] Manso AP, Marzo FF, Mujika MG, Barranco J, Lorenzo A. Numerical analysis of the influence of the channel cross-section aspect ratio on the performance of a PEM fuel cell with serpentine flow field design. Int J Hydrog Energy 2011;36(11):6795–808. http://dx.doi.org/10.1016/j.ijhydene.2011.02.099.

[33] Selvaraj AS, Rajagopal TKR. Numerical investigation on the effect of flow field and landing to channel ratio on the performance of PEMFC. Int J Energy Res 2020;44(1):171–91. http://dx.doi.org/10.1002/er.4885.

[34] Maximilian Schmitz MBuSG. FC COLD START: PEM-FC cold start simulation: Forschungsbericht. 2023.
[35] Schmitz M. Numerische und experimentelle untersuchung von froststarts und verschiedenen froststartmethoden von PEM-brennstoffzellenstacks (Ph.D. thesis), RWTH Aachen University; 2024, http://dx.doi.org/10.18154/RWTH-2024-05813.
[36] Schmitz M, Welker F, Tinz S, Bahr M, Gössling S, Kaimer S, Pischinger S. Comprehensive investigation of membrane sorption and CFD modeling of a tube membrane humidifier with experimental validation. Int J Hydrog Energy 2023;48(23):8596–612. http://dx.doi.org/10.1016/j.ijhydene.2022.11.081.
[37] Nitta I, Hottinen T, Himanen O, Mikkola M. Inhomogeneous compression of PEMFC gas diffusion layer. J Power Sources 2007;171(1):26–36. http://dx.doi.org/10.1016/j.jpowsour.2006.11.018.
[38] Hottinen T, Himanen O, Karvonen S, Nitta I. Inhomogeneous compression of PEMFC gas diffusion layer. J Power Sources 2007;171(1):113–21. http://dx.doi.org/10.1016/j.jpowsour.2006.10.076.
[39] Terrey F. Untersuchungen zur alterungsbeständigkeit von dichtungen in PEM-brennstoffzellen (Ph.D. thesis), Fakultät für Ingenieurwissenschaften Informatik und Psychologie der Universität Ulm; 2015.
[40] El-kharouf A, Steinberger-Wilckens R. The effect of clamping pressure on gas diffusion layer performance in polymer electrolyte fuel cells. Fuel Cells 2015;15(6):802–12. http://dx.doi.org/10.1002/fuce.201500088.
[41] Irmscher P. Mechanical properties of polymer electrolyte membrane fuel cells. RWTH Aachen University; 2019, http://dx.doi.org/10.18154/RWTH-2019-09199.
[42] Mason TJ, Millichamp J, Neville TP, El-kharouf A, Pollet BG, Brett DJ. Effect of clamping pressure on ohmic resistance and compression of gas diffusion layers for polymer electrolyte fuel cells. J Power Sources 2012;219:52–9. http://dx.doi.org/10.1016/j.jpowsour.2012.07.021.
[43] Zhou P, Wu CW, Ma GJ. Influence of clamping force on the performance of PEMFCs. J Power Sources 2007;163(2):874–81. http://dx.doi.org/10.1016/j.jpowsour.2006.09.068.
[44] Qiu D, Peng L, Lai X, Ni M, Lehnert W. Mechanical failure and mitigation strategies for the membrane in a proton exchange membrane fuel cell. Renew Sustain Energy Rev 2019;113:109289. http://dx.doi.org/10.1016/j.rser.2019.109289.
[45] Liu Y, Kohrn M, Wick M, Pischinger S. Optimization of the bipolar plate rib structure in proton exchange membrane fuel cells with an analytical method. Int J Hydrog Energy 2022;47(40):17683–98. http://dx.doi.org/10.1016/j.ijhydene.2022.03.108.
[46] Fırat AE. Mechanical analysis of PEM fuel cell stack design (Ph.D. thesis), Universität Duisburg-Essen; 2016.
[47] Bird RB, I. Stewart W. Transport phenomena. 2a ed, revisada ed.. New York: J. Wiley; 2007.
[48] Siemens. SarCCM+ 2406: Usert guide. 2024, URL https://plm.sw.siemens.com/de-DE/simcenter/fluids-thermal-simulation/star-ccm/.
[49] Bear J. Dynamics of fluids in porous media. Dover books on physics and chemistry, Repr. [d. Ausg.], New York, American Elsevier Pub., 1972, with corr ed.. New York: Dover Publ; 1988, URL http://www.loc.gov/catdir/description/dover032/87034940.html.
[50] Shen L, Chen Z. Critical review of the impact of tortuosity on diffusion. Chem Eng Sci 2007;62(14):3748–55. http://dx.doi.org/10.1016/j.ces.2007.03.041.
[51] Yu Z, Carter RN, Zhang J. Measurements of pore size distribution, porosity, effective oxygen diffusivity, and tortuosity of PEM fuel cell electrodes. Fuel Cells 2012;12(4):557–65. http://dx.doi.org/10.1002/fuce.201200017.
[52] Vetter R, Schumacher JO. Experimental parameter uncertainty in proton exchange membrane fuel cell modeling. Part I: Scatter in material parameterization. J Power Sources 2019;438:227018. http://dx.doi.org/10.1016/j.jpowsour.2019.227018.
[53] Bruggeman DAG. Berechnung verschiedener physikalischer konstanten von heterogenen Substanzen. I. Dielektrizitätskonstanten und leitfähigkeiten der mischkörper aus isotropen substanzen. Ann Phys, Lpz 1935;416(7):636–64. http://dx.doi.org/10.1002/andp.19354160705.
[54] Huang H, Ayoub J. Applicability of the Forchheimer Equation for Non-Darcy flow in porous media. SPE J 2008;13(01):112–22. http://dx.doi.org/10.2118/102715-PA.
[55] Leverett MC. Capillary behavior in porous solids. Trans AIME 1941;142(01):152–69. http://dx.doi.org/10.2118/941152-G.
[56] Wu H, Li X, Berg P. On the modeling of water transport in polymer electrolyte membrane fuel cells. Electrochim Acta 2009;54(27):6913–27. http://dx.doi.org/10.1016/j.electacta.2009.06.070.
[57] Faraday M. VI. Experimental researches in electricity.-Seventh Series. Philos Trans R Soc Lond 1834;124:77–122. http://dx.doi.org/10.1098/rstl.1834.0008.
[58] Strong FC. Faraday's laws in one equation. J Chem Educ 1961;38(2):98. http://dx.doi.org/10.1021/ed038p98.
[59] Wu H, Berg P, Li X. Non-isothermal transient modeling of water transport in PEM fuel cells. J Power Sources 2007;165(1):232–43. http://dx.doi.org/10.1016/j.jpowsour.2006.11.061.
[60] Barbir F. PEM fuel cells: Theory and practice. Sustainable world, 1st ed.. Burlington: Elsevier Science & Technology; 2005, URL https://ebookcentral.proquest.com/lib/kxp/detail.action?docID=269935.
[61] Gasteiger H, Gu W, Makharia R, Mathias M. Tutorial: catalyst utilization and mass transfer limitations in the polymer electrolyte fuel cell. In: The 2003 electrochemical society meeting.
[62] Parthasarathy A, Srinivasan S, Appleby AJ, Martin CR. Temperature dependence of the electrode kinetics of oxygen reduction at the Platinum/Nafion® interface—A microelectrode investigation. J Electrochem Soc 1992;139(9):2530–7. http://dx.doi.org/10.1149/1.2221258.
[63] Sun W, Peppley BA, Karan K. An improved two-dimensional agglomerate cathode model to study the influence of catalyst layer structural parameters. Electrochim Acta 2005;50(16–17):3359–74. http://dx.doi.org/10.1016/j.electacta.2004.12.009.
[64] Springer TE, Zawodzinski TA, Gottesfeld S. Polymer electrolyte fuel cell model. J Electrochem Soc 1991;138(8):2334–42. http://dx.doi.org/10.1149/1.2085971.
[65] Ye Q, van Nguyen T. Three-dimensional simulation of liquid water distribution in a PEMFC with experimentally measured capillary functions. J Electrochem Soc 2007;154(12):B1242. http://dx.doi.org/10.1149/1.2783775.
[66] Scholz H. Modellierung und untersuchung von flutungsphänomenen in niedertemperatur-PEM-brennstoffzellen (Ph.D. thesis).
[67] Ge S-H, Yi B-L. A mathematical model for PEMFC in different flow modes. J Power Sources 2003;124(1):1–11. http://dx.doi.org/10.1016/S0378-7753(03)00584-6.
[68] Maxwell JC. Treatise on electricity and magnetism: Vol 1. Repr., unabridged 3. ed., [Clarendon Press, Oxford 1891] ed.. Oxford: Oxford University Press; 1892.
[69] Maxwell JC. A treatise on electricity and magnetism: Vol 2. Unabridged 3. ed., republ ed.. New York: Dover Publ; 1892.
[70] Rautio JC. Maxwell's legacy. IEEE Microw Mag 2005;6(2):46–53. http://dx.doi.org/10.1109/MMW.2005.1491266.
[71] Zhou P, Wu CW, Ma GJ. Contact resistance prediction and structure optimization of bipolar plates. J Power Sources 2006;159(2):1115–22. http://dx.doi.org/10.1016/j.jpowsour.2005.12.080.
[72] Wang C-Y. Fundamental models for fuel cell engineering. Chem Rev 2004;104(10):4727–65. http://dx.doi.org/10.1021/cr020729l.
[73] Tabuchi Y, Shiomi T, Aoki O, Kubo N, Shinohara K. Effects of heat and water transport on the performance of polymer electrolyte membrane fuel cell under high current density operation. Electrochim Acta 2010;56(1):352–60. http://dx.doi.org/10.1016/j.electacta.2010.08.070.
[74] Corda G, Fontanesi S, d'Adamo A. Methodology for PEMFC CFD simulation including the effect of porous parts compression. Int J Hydrog Energy 2022;47(32):14658–73. http://dx.doi.org/10.1016/j.ijhydene.2022.02.201.
[75] Liu Y. A model for proton exchange membrane fuel cells considering polarization effects of liquid water (Ph.D. thesis), RWTH Aachen University; 2023, http://dx.doi.org/10.18154/RWTH-2023-04076.
[76] Kohrn M, Liu Y, Wick M, Pischinger S. A scalable PEM fuel cell model for coupled mechanical and electrochemical analysis based on an analytical approach. Int J Hydrog Energy 2024;51:1539–59. http://dx.doi.org/10.1016/j.ijhydene.2023.08.165.
[77] Blank J, Deb K. Pymoo: Multi-Objective optimization in Python. IEEE Access 2020;8:89497–509. http://dx.doi.org/10.1109/ACCESS.2020.2990567.
[78] Kohrn M. Entwicklung einer simulationsumgebung zur gekoppelten mechanischen und elektrochemischen untersuchung und optimierung von PEM-brennstoffzellen (Ph.D. thesis), 2025, (in preparation).